Available online at www.sciencedirect.com
ScienceDirect
Journal of Solid State Chemistry 181 (2008) 245–252
JOURNAL OF SOLID STATE CHEMISTRY
www.elsevier.com/locate/jssc

Studies on the magnetism of cobalt ferrite nanocrystals synthesized by hydrothermal method

Lijun Zhao[a], Hongjie Zhang[a,*], Yan Xing[a,b], Shuyan Song[a,b], Shiyong Yu[a,b], Weidong Shi[a,b], Xianmin Guo[a,b], Jianhui Yang[a,b], Yongqian Lei[a,b], Feng Cao[a,b]

[a]*Key Laboratory of Rare Earth Chemistry and Physics, Changchun Institute of Applied Chemistry, Chinese Academy of Sciences, Changchun 130022, PR China*
[b]*Graduate School of the Chinese Academy of Sciences, Beijing, PR China*

Received 27 August 2007; received in revised form 24 October 2007; accepted 27 October 2007
Available online 17 November 2007

Abstract

Fe–Co/$CoFe_2O_4$ nanocomposite and $CoFe_2O_4$ nanopowders were prepared by the hydrothermal method. The structure of magnetic powders were characterized by X-ray diffraction diffractometer (XRD), field emission scanning electron microscopy (FE-SEM), transmission electron microscopy (TEM), thermal gravity analysis (TGA) and differential thermal analysis (DTA) analysis, X-ray photoelectron spectrometry (XPS), and Fourier transform infrared spectra (FTIR) techniques, while magnetic properties were determined by using a vibrating sample magnetometer (VSM) at room temperature. The effects of hydrothermal reaction conditions on magnetic properties were also discussed in details. The values of saturation magnetization (M_s) and coercive fore (H_c) for Fe–Co/$CoFe_2O_4$ nanocomposite are 113 emu/g and 1.4 kOe, respectively. Furthermore, $CoFe_2O_4$ ferrite with a single-domain critical size of 70 nm was fabricated by controlling the hydrothermal reaction conditions carefully, which presents high coercive force (ca. 4.6 kOe) and high squareness ratio (ca. 0.65). One interesting thing is M_s value of $CoFe_2O_4$ ferrite with a diameter of 40 nm is 86 emu/g which is comparable to that of the bulk counterpart.

Keywords: $CoFe_2O_4$ ferrite; Saturation magnetization; Coercive force

1. Introduction

$CoFe_2O_4$ ferrite has large magnetocrystalline anisotropy and reasonable magnetization, as potential predominant magnetic and electrical resistive materials, which has been applied in high-density magnetic recording media, high-performance electromagnetic and spintronic devices [1,2]. To date, many methods have been developed for preparing $CoFe_2O_4$ ferrite nanomaterials with various magnetism, for instance, sonochemical reactions [3], mechanochemical synthesis [4–6], hydrolysis of precursors [7,8], flow injection synthesis [9], aqueous co-precipitation [10,11] and hydrothermal method [12]. Among them, hydrothermal synthesis is an attractive method owing to the higher yield and simplicity [13,14]. When the solution reaction proceeded under N_2 atmosphere, Fe–Co/$CoFe_2O_4$ composite could be fabricated, conversely, $CoFe_2O_4$ ferrite was obtained. Fe–Co/$CoFe_2O_4$ composite has attracted considerable attention due to their novel physical and chemical properties, and potential application in catalytic behaviors [15], and magnetic properties. [16,17].

For nanoscaled $CoFe_2O_4$ particles, the room temperature coercivity values were reported to be 500–2000 Oe, which is far lower than the theoretically estimated one [18]. At different reaction conditions, many possible phases may exist, such as ferrihydrite ($Fe_5HO_8 \cdot 4H_2O$), akagenite (β-FeOOH), and $Fe(OH)_3$, etc., so the magnetic properties of final products are reduced. It is well known that the reaction conditions are important in determining the magnetic properties of prepared samples. However, it is not clearly known how the reaction conditions affect the magnetic properties of the prepared samples during the hydrothermal process. Hence hydrothermal conditions,

*Corresponding author. Fax: +86 431 85698041.
E-mail address: hongjie@ns.ciac.jl.cn (H. Zhang).

0022-4596/$ - see front matter © 2007 Elsevier Inc. All rights reserved.
doi:10.1016/j.jssc.2007.10.034

such as addition of surfactant, reaction time, concentration of alkali, types of alkali, and so on, were adjusted carefully.

2. Experimental section

2.1. Chemicals

Cobalt chloride hexahydrate ($CoCl_2 \cdot 6H_2O$), ferrous sulfate heptahydrate ($FeSO4 \cdot 7H_2O$), iron nitrate nonahydrate ($Fe(NO_3)_3 \cdot 9H_2O$), cobalt nitrate hexahydrate ($Co(NO_3)_3 \cdot 6H_2O$), potassium hydroxide (KOH), sodium hydroxide (NaOH), 28 wt% ammonia ($NH_3 \cdot H_2O$) and cetyltrimethyammoniumbromide (CTAB) were used for the synthesis of cobalt ferrites. The chemicals were all of analytical reagent grade, and were used without further purification.

2.2. Sample preparation

0.6 mmol of $FeSO_4 \cdot 7H_2O$, 0.3 mmol of $CoCl_2 \cdot 6H_2O$, and 3 mmol CTAB were dissolved in 50 ml distilled water to form a transparent solution followed by the addition of 10 ml of distilled water containing 0.15 mol of KOH. Then, the deep green solution (with N_2 flow) or brown solution (without N_2 flow) was transferred to autoclaves. The autoclaves were sealed and put into an oven heated at 140 °C for 3 h. The autoclaves were taken out and cooled naturally to room temperature. The final products were washed with water and ethanol for several times to remove impurities before the characterizations.

2.3. Sample characterization

X-ray diffraction (XRD patterns were recorded on a Rigaku-D/max 2500 V X-ray diffractometer equipped with a source of Cu Kα radiation ($\lambda = 1.54178$ Å) at a step width of 0.02°. The morphologies and structures of the as-synthesized ferrite products were observed with a field emission scanning electron microscopy (FE-SEM) and a transmission electron microscopy (TEM). All the samples for the FE-SEM and TEM characterization were prepared by directly transferring the suspended products to the ITO glass slide and standard copper grid coated with an amorphous carbon film, respectively. X-ray photoelectron spectrometry (XPS) analysis was performed on a VG ESCA MKII. Thermal gravity analysis (TGA) and differential thermal analysis (DTA) analysis were made on a SDT 2960 analyzer (Shimadzu, Japan) from 40 to 800 °C at a heating speed of 5 °C/min under air atmosphere. Fourier transform infrared spectra (FTIR) were measured with a Bruker Vertex 70 Spectrophotometer within the wave number range of 4000–360 cm^{-1} using KBr pressed pellet technique. Room-temperature hysteretic loops were collected on a VSM-7300 vibrating sample magnetometer (VSM) (Lakeshore, USA).

3. Results and discussion

It was found that inert atmosphere plays a key role foe the preparation of Fe–Co/$CoFe_2O_4$ nano-composite. If the whole reaction was protected by N_2, the Fe–Co/$CoFe_2O_4$ composite was prepared, otherwise only could obtain $CoFe_2O_4$ nanopowders. Fe–Co/$CoFe_2O_4$ nanocomposite and $CoFe_2O_4$ nanocrystals can be successfully synthesized by hydrothermal method, when $FeSO_4 \cdot 7H_2O$ was used as the iron source. Different synthetic conditions for the fabrication of Fe–Co/$CoFe_2O_4$ composite and $CoFe_2O_4$ ferrites are listed in Table 1, and the relations between synthetic conditions and magnetic properties are commented on in the following paragraphs.

3.1. Structural analysis

XRD patterns of Fe–Co/$CoFe_2O_4$ nanocomposite and representative $CoFe_2O_4$ nanopowders were shown in Fig. 1. Fig. 1(1*) is the XRD pattern of Fe–Co/$CoFe_2O_4$

Table 1
Synthesis conditions for the preparation of $CoFe_2O_4$ nanocrystals

Sample	Salt	Temperature (°C)	Time (h)	CTAB (mmol)	Precipitator (mmol)
1* (N_2)	Fe^{2+}, Co^{2+}	140	3	3	KOH = 0.15
1*-a(N_2)	Fe^{2+}, Co^{2+}	180	24	3	KOH = 0.15
2*	Fe^{2+}, Co^{2+}	140	3	0	KOH = 0.15
3*	Fe^{2+}, Co^{2+}	140	3	2	KOH = 0.15
4*	Fe^{2+}, Co^{2+}	140	3	3	KOH = 0.15
5*	Fe^{2+}, Co^{2+}	140	3	4	KOH = 0.15
6*	Fe^{2+}, Co^{2+}	140	3	5	KOH = 0.15
7*	Fe^{2+}, Co^{2+}	140	5	3	KOH = 0.15
8*	Fe^{2+}, Co^{2+}	140	7	3	KOH = 0.15
9*	Fe^{2+}, Co^{2+}	140	24	3	KOH = 0.15
10*	Fe^{2+}, Co^{2+}	140	3	3	KOH = 0.15
11*	Fe^{2+}, Co^{2+}	140	3	3	KOH = 0.25
12*	Fe^{2+}, Co^{2+}	140	3	3	$NH_3 \cdot H_2O$ = 0.15
13*	Fe^{2+}, Co^{2+}	140	3	3	NaOH = 0.15
14*	Fe^{3+},Co^{2+}	140	3	3	KOH = 0.15

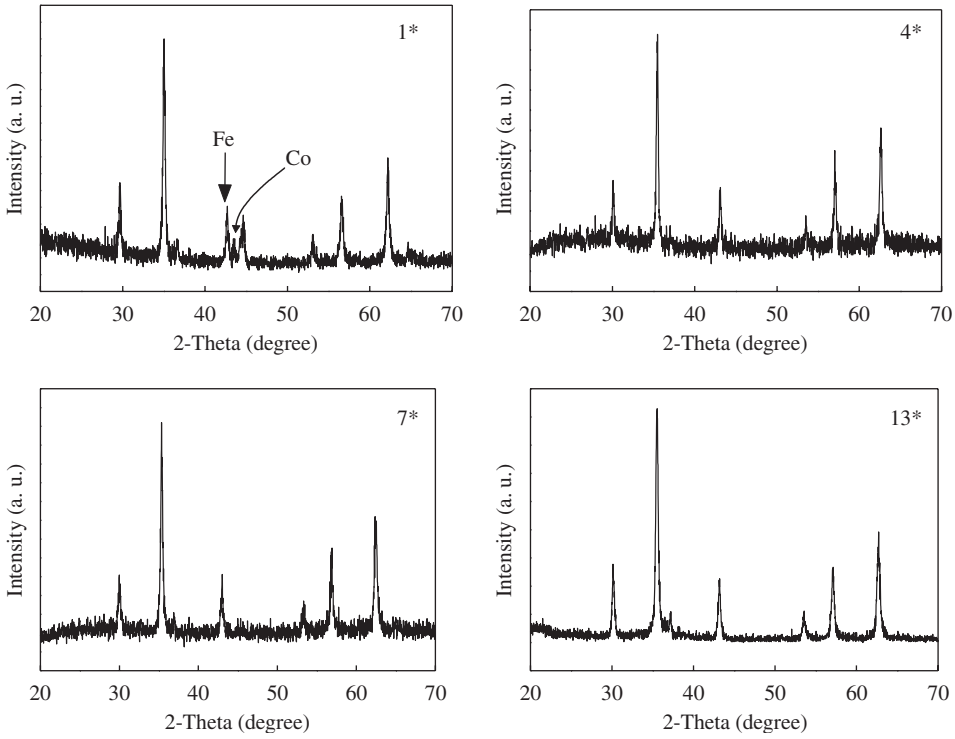

Fig. 1. XRD patterns of samples 1*, 4*, 7* and 13*.

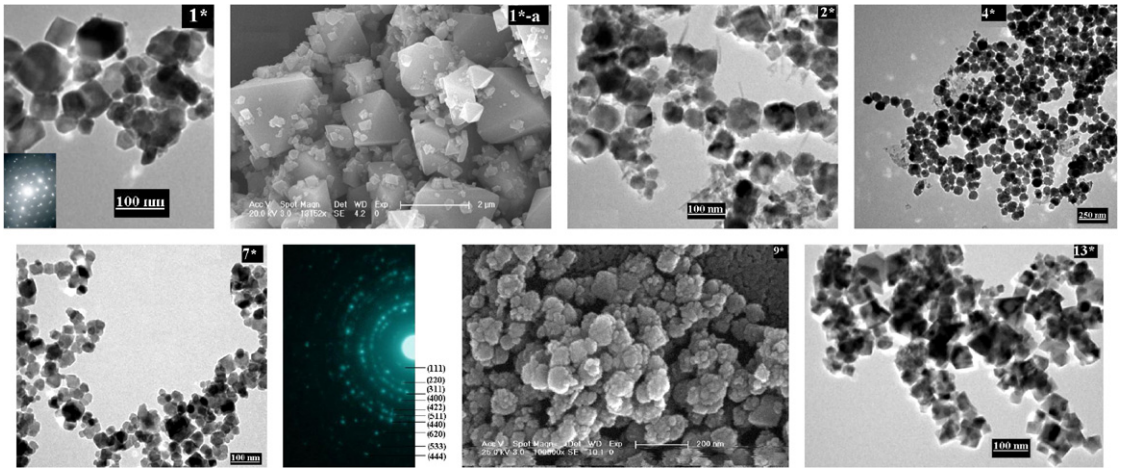

Fig. 2. TEM images of samples 1*, 2*, 4*, 7* and 13*, the diffraction images of sample 7* and SEM photos of samples 1*-a and 9*.

nanocomposite. For metal Co, the peak can be indexed to face center cubic structure with space group Fm-3 m (JCPDS card No. 15-0806). For metal Fe, the peak can be indexed to body center cubic structure with space group Im-3 m (JCPDS card No. 06-0696). All the diffraction peaks in the XRD patterns of Fig. 1 (4*, 7* and 13*) can be indexed to face center cubic structure of cobalt ferrite according to JCPDS card No. 22-1086.

Fig. 2 (1* and 1*-a) indicate TEM and SEM images of the samples. From the TEM image of sample 1*, we can observe hexagons with diameters about 50–90 nm and irregular small particles with diameters about 15 nm. The hexagons are the projections of octahedra. Both of them may be spinel phase. The metal alloys could be in the inner of spinel particles, so they can consist in sample steadily. The inset in Fig. 1 (1*) is the electronic diffraction image, and the nature of single crystal can be revealed. From SEM photo of sample 1*-a, the crystallites are composed of octahedra and small particles with crystallite sizes of ca. 1.5 μm and 150 nm. In water solution, quick nucleation and quick growth rate may lead directly to the size distribution in a broader scope. Here we successfully prepared single-crystal Fe–Co/$CoFe_2O_4$ nano- and micro-composites through controlling hydrothermal reaction time and reaction temperature.

According to Gibbs–Wulff's theorem [19], higher surface tension faces tend to grow along its normal direction and eventually disappear from the final appearance. The crystal structure analysis shows that $CoFe_2O_4$ ferrite adopts a face-centered cubic crystal structure and a general sequence for the surface energies of $CoFe_2O_4$ nanocrystal structure is $\gamma\{1\,1\,1\}<\gamma\{1\,0\,0\}<\gamma\{1\,1\,0\}$ can be easily deduced from the distances between these three faces and the central Wulff's point [19,20]. The $\gamma\{1\,1\,1\}$ becomes the lowest among the three kinds of faces (1 1 1), (1 0 0), and (1 1 0). It is known that single-crystal particles usually have specific shapes because a single-crystal particle has to be enclosed by crystallographic facets that have lower energy [21–23]. The octahedra were enclosed by (1 1 1) planes, so octahedral structure is favorable over other possible crystal forms.

Fig. 2 (2*, 4*, 7*, 9* and 13*) are the TEM and SEM photos of cobalt ferrite nanocrystals prepared at different hydrothermal reaction conditions. Besides cobalt ferrite, some extra phases can also be observed from the Fig. 2 (2*), which are akagenite (β-FeOOH) phase. Herein, nanorods are β-FeOOH, while the analogous spheres are cobalt ferrite with diameters of 70 nm. In this synthetic condition, formation of β-FeOOH phase may be due to the lower alkaline concentration. At such an alkaline concentration, pure cobalt ferrite could be prepared by prolonging the reaction time to 6 h. The appearance of sample 4* is regular spheres with diameter of 70 nm (Fig. 2 (4*). Interestingly, the regular spheres are linked in short range, and the longest chain could reach several hundred nanometers. The formation of $CoFe_2O_4$ particles chains may be attributed to magnetic dipole–dipole interaction between neighboring particles. Comparing sample 2* with sample 4*, we concluded that CTAB could confine the formation of β-FeOOH. A large number of irregular particles with diameters of 40 nm can be seen from Fig. 2 (7*). Sample 9* with particles sizes about 100 nm formed by some small particles (ca. 20 nm), which indicates that CTAB could slow down the growth rate of $CoFe_2O_4$ ferrite nanoparticles. The morphology of sample 13* exhibits a majority of cubes and a minority of spheres, and their particle sizes are about 35 nm. In the same synthetic conditions, we found that prolonging of hydrothermal reaction time or NaOH as precipitator are in favor of formation of single-phase cobalt ferrite nanocrystals.

Gedde et al. [24] prepared cobalt ferrite according to the "chemie-douce" method. They reported that the cobalt ferrite nanoparticles with stoichiometric composition were a mixture of cubical and spherical shapes; nanoparticles with less than the stoichiometric cobalt content had an irregular morphology, whereas nanoparticles with greater than the stoichiometric concentration of cobalt were predominantly spherical. Sample 2* contains some β-FeOOH phase, which can be proved by XRD patterns and TEM images obviously. And there is also trace β-FeOOH in sample 4*, which can be observed from TEM image. These phenomena indicate that the contents of cobalt ions in samples 2* and 4* are larger than stoichiometric contents of cobalt ions, hence the morphologies of samples 2* and 4* show spherical shape. Samples 7* and 13* have similar particle sizes about 40 nm, however, both of them are smaller than the particle size of sample 4*. As well known, hydrothermal method is a wonderful reaction process, and unpredictable experimental phenomena may happen at high temperature and high-pressure conditions. The nuance of morphology and chemical composition for samples maybe the main reasons for different crystallite sizes. Furthermore, diffraction image of sample 7* shows that the sample has well crystallization. On the basis of TEM images, it can be concluded that the increase of alkaline concentration, hydrothermal time or hydrothermal temperature is in favor of the formation of single-phase and well-crystallization cobalt ferrites.

XPS spectra and DTA-TGA were used to further prove whether single-phase cobalt ferrites were fabricated. XPS spectra given in Fig. 3 display binding energies (BEs) assigned to Fe2p and Co2p on the surface of $CoFe_2O_4$ ferrites. The characteristic peaks of Fe^{2+} ions, metal Fe and Co are not observed, which indicates that there are only Fe^{3+} and Co^{2+} ions on the surface of $CoFe_2O_4$ ferrite. XPS could collect only 3 nm surface depth for inorganic compound. So we guess that there are some

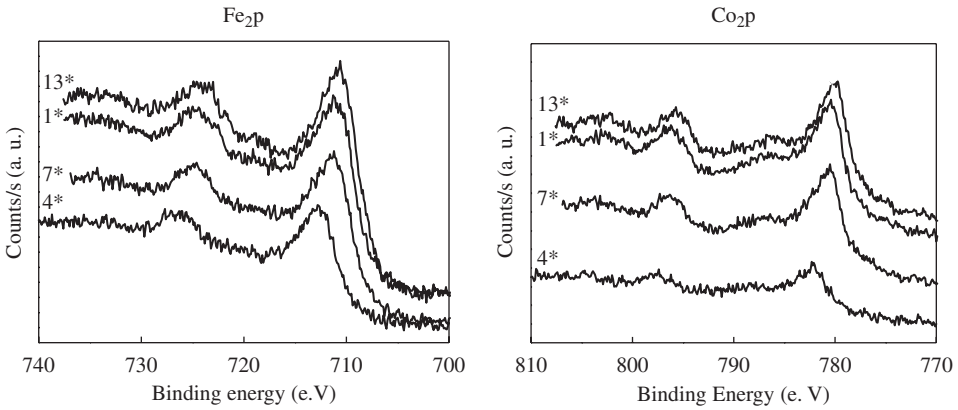

Fig. 3. XPS spectra of samples 1*, 4*, 7* and 13*.

differences between the surface and the inner chemical compositions.

The BEs of Fe2p and Co2p were listed in Table 2. For sample 13*, the BEs of Fe2p and Co2p are ascribed to the featured BEs of Fe^{3+} and Co^{2+} ions in $CoFe_2O_4$ ferrite. $CoFe_2O_4$ ferrite nanoparticles of sample 13* with stoichiometric composition could be proved by the XPS characterization. For samples 1* and 7*, the BE of Fe2p is ascribed to that of Fe^{3+} in Fe_2O_3, and the BE of Co2p is ascribed to that of CoO. Sample 1* may contain metals of Fe and Co. For sample 4*, the presence of trace β-FeOOH on the surface of $CoFe_2O_4$ ferrites may lead to the chemical shift of the BEs of Fe2p and Co2p.

Fig. 4 shows the DTA-TG curves of samples. For sample 1*, there is an exothermic peak at 200 °C, which is attributed to the oxidation of metal alloy. The transformation of magnetite into maghemite corresponds to the peak at around 248 °C (exothermic peak). There is a little magnetite in Fe–Co/$CoFe_2O_4$ composite, because of the disproportion reaction. It is well known that magnetite can be oxidized to maghemite, which can be further transformed into hematite at a higher temperature [25]. The exothermic peak at 461 °C is owing to the final phase transformation of maghemite into hematite [26]. TG curve of sample 1* displays a weight loss from the room temperature to 248 °C and a weight gain above 248 °C. The complex behavior results from the simultaneous dehydration of the powders and oxidation of Fe, Co and Fe_3O_4. The competition between dehydration and oxidation prevents us from evaluating the weight gain corresponding to Fe and Co alloy oxidation in Fe–Co/$CoFe_2O_4$. For sample 4*, an exothermic peak at 233 °C in the DTA curve is due to the transformation of β-FeOOH into Fe_2O_3. The other very weak endothermic peak at 340 °C in the DTA curve is ascribed to the transformation of Fe_2O_3 into spinel phase. For sample 7*, there is an exothermic peak at 211 °C in the DTA curve, which may be owing to the oxidation of Fe_3O_4 into Fe_2O_3. An endothermic peak at 335 °C may be due to the transformation of oxides into spinel phase. We could not observe exothermic and endothermic peaks in the DTA curve for sample 13*, which may be a hint that the stoichiometric cobalt ferrite has been synthesized. The percentages of weight loss in TG curves for samples 4*, 7* and 13* are 6.058%, 4.243% and 1.832%, respectively. Surfactant in sample 4* is the main reason for large weight loss, and there is only dehydration in stoichiometric cobalt ferrite with so less weight loss.

By investigating the FTIR spectra of the samples, we may judge the iron ions contents on A- and B-sites. Then, magnetic properties can be evaluated non-quantitatively, because the distribution of metals ions on A- and B-sites decides the magnetic properties of ferrite. Fig. 5 shows the

Table 2
Binding energy (BE) of Fe2p and Co2p

	1*	4*	7*	13*
Fe2p3/2	711.3	712.7	711.2	710.5
Co2p3/2	780.4	782.3	780.5	779.7

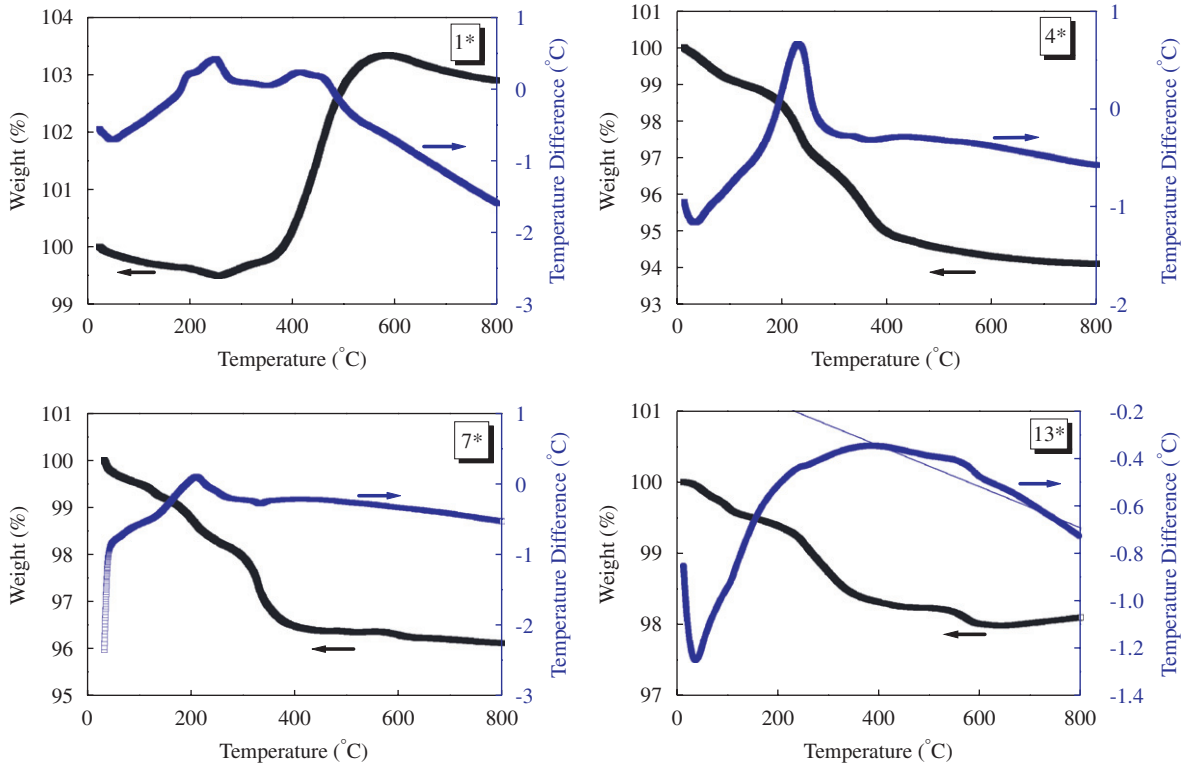

Fig. 4. DTA-TGA curves for samples 1*, 4*, 7* and 13* at air atmospheres.

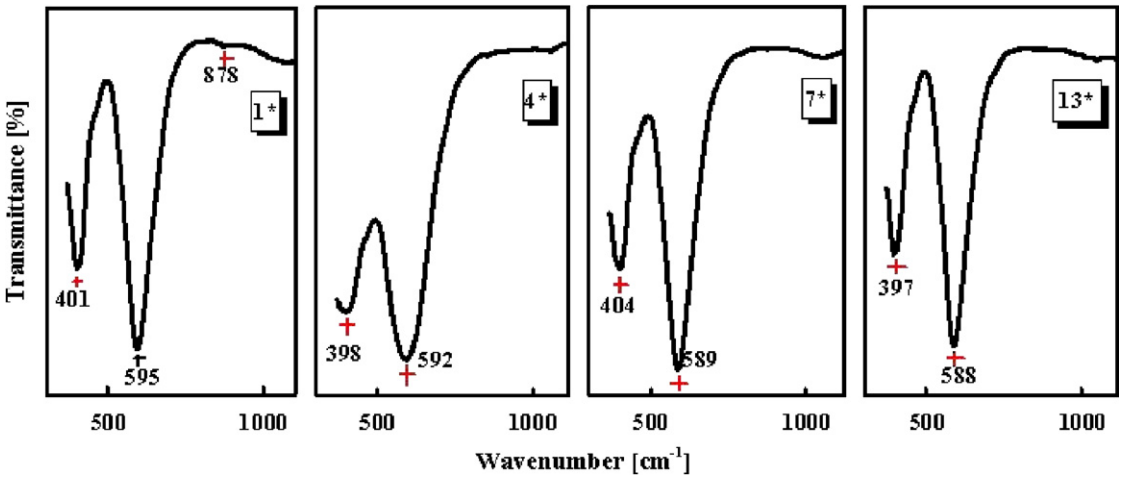

Fig. 5. FTIR of samples 1*, 4*, 7* and 13*.

FTIR spectra of samples. The bands at 401, 398, 404 and 397 cm^{-1} are assigned to the vibration modes of octahedral groups (Fe^{3+}–O^{2-}), while bands at 595, 592, 589 and 588 cm^{-1} are due to the stretching vibrations of the tetrahedral groups (Fe^{3+}–O^{2-}) [27]. The presence of Fe and Co alloys in sample 1* may be responsible for the stretching vibrations at 878 cm^{-1}. Compared with sample 13*, both the bands corresponding to A (tetrahedron) and B (octahedron) sites for sample 1* shift to high wave numbers. This may be owing to the presence of Fe–Co alloys in cobalt ferrite. Compared to sample 13*, the band corresponding to A-sites for sample 4* shifts to high wave number. The r_{Fe}^{3+} (0.64 Å) is smaller than r_{Co}^{2+} (0.74 Å), so the content of Fe^{3+} ions on A-sites for sample 4* is larger than that for sample 13*. The band corresponding to B-sites for sample 7* shifts to high wave number in comparison with the counterpart of sample 13*, indicating that the content of Fe^{3+} ions on B-sites for sample 7* is larger than that for sample 13*. By FTIR analysis, the contents of Fe^{3+} ions on A- and B-sites can be estimated cursorily.

3.2. Magnetic properties

The effects of different reaction conditions on the magnetic properties can be observed intuitively from Fig. 6. The magnetization curves for the samples 10* exhibit "constricted" hysteretic loops. A magnetic sample that is a mixture of hard and soft magnetic material could give rise to this kind of magnetization curves, for example, the hard magnetic $CoFe_2O_4$ particles contain some soft magnetic iron oxide associated them. Sample 2*, 4*, 9* and 10* are far from saturation. For a collection of nanocrystals with random crystallographic orientations, the applied fields rotate the magnetic moments into the direction of the field at saturation, which may be away from the magnetic easy axis of the particles. This spin rotation could be the reason for the relatively slow rise in the magnetization at higher applied fields. The magnetic parameters of samples obtained from hysteresis loops are listed in Table 3.

Compared sample 1* with sample 1*-a, neither the increase of hydrothermal temperature nor hydrothermal time makes the magnetic properties especially outstanding. This indicates that Fe content is the key factor to determine the magnetic properties, but the crystal structure can become more perfect by improving hydrothermal reaction temperature and time. The magnetic properties of Fe–Co/$CoFe_2O_4$ synthesized by hydrothermal method are consistent with those of Fe–Co/$CoFe_2O_4$ synthesized by traditional disproportion method [28].

The M_s value of sample 2* is relatively low, because of the existence of some FeOOH. Results show that only trace FeOOH consists in samples 3*, 4*, 5* and 6*. Therefore, we can infer that the introduction of CTAB could confine the formation FeOOH. CTAB is cationic surfactant, thus the ion pairs of $[Fe(OH)_6]^{3-}$-CTA^+ could be formed by electrostatic effect in the alkaline solution. The ion pairs of $[Fe(OH)_6]^{3-}$-CTA^+ inhibit the transformation of $[Fe(OH)_6]^{3-}$ to FeOOH. For sample 4*, its H_c value reaches 4.6 kOe, and M_s value is 55 emu/g. Such a high coercive force proves that the particle sizes of sample 4 * are at the critical size of a single domain. When the size of a ferro- or ferri-magnet decreases to a certain critical value r_c, the particles change from a state with multiple magnetic domains to one with a single domain. When the particle size is much larger than the critical size of a single domain, the coercivity is determined by magnetic displacement, so the value of coercive force is small. When the particle size is reduced to the critical size of single domain, the coercivity is determined by magnetic domain rotation, so the coercivity reaches the maximum. When the particle size is less than the critical size of a single domain, the coercivity will decrease for the existence of superparamagnetism. Here the particle size of sample 4* is about 70 nm, which is consistent with the critical size of a single-domain particle of $CoFe_2O_4$ ferrite at room temperature, based on the coercivity measurements [29]. It is interesting to note that

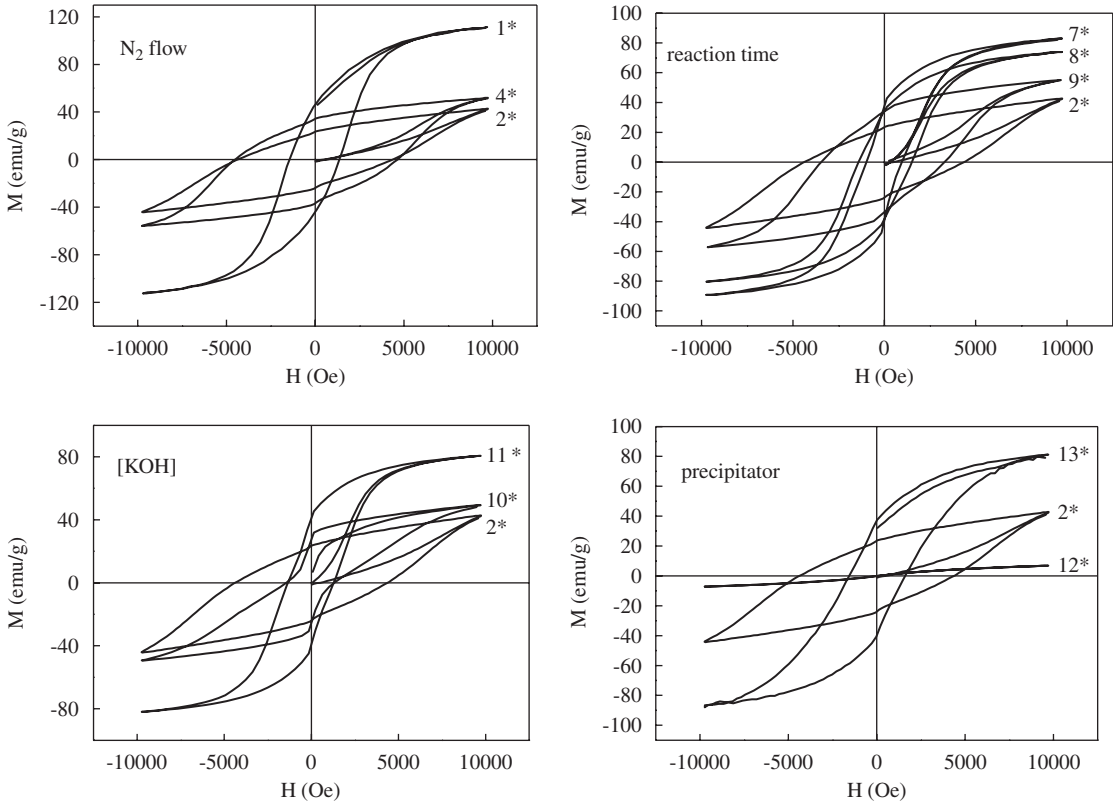

Fig. 6. Effects of different reaction conditions on the hysteresis loops.

Table 3
Magnetic parameters of samples

Sample	M_s (emu/g)	M_r (emu/g)	H_c (Oe)	M_r/M_s
1*	113	47	1438	0.41
1*-a	110	41	1065	0.37
2*	44	23	4365	0.52
3*	55	34	4000	0.62
4*	55	36	4556	0.65
5*	56	34	3513	0.61
6*	58	35	3273	0.6
7*	86	40	978	0.44
8*	80	38	1512	0.48
9*	57	35	3422	0.61
10*	49	27	1518	0.55
11*	82	41	1345	0.50
12*	7	0	0	0
13*	84	39	1619	0.45
14*	15	3	945	0.2

the H_c value of 4.6 kOe for the 70 nm of $CoFe_2O_4$ particles at room temperature is very high and also close to the theoretical value of 5.3 kOe. For samples 3*, 4*, 5* and 6*, the values of squareness ratio (M_r/M_s) are in the range of 0.6–0.65, which indicates that the system consists of randomly oriented equiaxial particles with cubic magnetocrystalline anisotropy [30]. In this case, the magnetization mainly depends on the magnetic domain rotation, so the coercivity can be calculated by Stoner-Wohlfarth theory, $H_c = 2K/(\mu_0 M_s)$, where K is magnetocrystalline anisotropy constant and μ_0 is vacuum permeability. It clearly shows that the H_c and the M_s are in reverse proportion, that is to say, the higher H_c leads to the lower M_s for the samples with cubic magnetocrystalline anisotropy.

The hydrothermal reaction time plays an important role in determining the magnetic properties. The M_s value of sample 7* ($M_s = 86$ emu/g) is comparable to that of $CoFe_2O_4$ bulk material, while its particle sizes are only 40 nm. For samples 8* and 9*, the prolonging in hydrothermal time leads to the decrease in M_s and the increase in H_c. And the analysis of FTIR suggests that the content of Fe^{3+} ions on B-sites for sample 7* is larger than that for sample 13*, that is to say, the magnetic properties are decided by the distributions of Fe^{3+} ions on A- and B-sites. The magnetic moment on the B-sites minus that on the A-sites leaves the total magnetic moment ($M = M_B$-M_A), as a result, the saturation magnetization of sample 7* is larger than that of sample 13*. The further increase in hydrothermal time affects directly the cationic distributions on A- and B-sites, therefore the values of M_s and H_c for sample 8* are changed. When the hydrothermal time prolongs to 24 h, both the values of M_s and H_c for sample 9* are similar to those for samples 5* and 6*. The magnetic properties of samples, which were prepared by the addition of CTAB into hydrothermal reaction, do not obviously change, but the morphology and particle sizes take place some diversification with the extension of hydrothermal time. This elucidates that the addition of surfactant plays an important role in deciding the cationic distributions on

A- and B-sites. The addition of CTAB could assure that the other reaction conditions do not influence the cationic distribution on A- and B-sites.

The concentration of KOH has some effects on the magnetic properties. To fix the other reaction conditions, the crystallization and nucleation can be promoted by the increase of the concentration of KOH. The values of saturation magnetization for samples 2* and 10* are smaller than that for sample 11* because of the presence of FeOOH in $CoFe_2O_4$ ferrite. High concentration of KOH can also inhibit the formation of FeOOH, while further increase of the concentration of KOH has little influence on the improvement of magnetic properties. In summary, $3\,mol\,L^{-1}$ may be a critical concentration for the preparation of single domain $CoFe_2O_4$ ferrite.

The effect of the precipitators on the magnetic properties of $CoFe_2O_4$ ferrite was also investigated. The single phase $CoFe_2O_4$ ferrite cannot be obtained by using a $3\,mol\,L^{-1}$ NH_4OH solution as the precipitator, but can be obtained by using a $3\,mol\,L^{-1}$ NaOH solution. This is because KCl and NaCl can promote the formation of $CoFe_2O_4$ ferrite. And the presence of NaCl greatly facilitates the hydrothermal reaction. However, the presence of NH_4Cl has little influence on the progress of hydrothermal reaction, and the weak magnetic properties of sample 12* may be owing to the formation of ferric and cobaltous complex compound. Magnetism is a kind of important property for complex compound because of the presence of the unpaired electrons.

When ferric salt was used as starting material, the sample had low saturation magnetization. In order to overcome this shortage, it needs to use ferrous salt as the original material, because the oxidation of ferrous ions would promote the ferrite nucleation and make the hydrothermal reaction easily occur.

4. Conclusions

We have synthesized Fe–Co/ $CoFe_2O_4$ nano-composite, bulk composite and single-phase $CoFe_2O_4$ nanopowders by changing the hydrothermal reaction temperature and time. For single-phase Fe–Co/ $CoFe_2O_4$ composite, octahedral structure is favorable over other crystal forms. And the nano-composite has high saturation magnetization (113 emu/g) and moderate coercivity (1438 Oe). The single-phase $CoFe_2O_4$ ferrites with critical size of 70 nm present high-coercive force (ca. 4.6 kOe) and high squareness ratio (ca. 0.65). Moreover, the saturation magnetization of the cobalt ferrite with a diameter of 40 nm bears comparison with that of the bulk counterpart. It is interesting that the presence of KCl or NaCl in the solution can promote the progress of hydrothermal reaction, while the presence of NH_4Cl does not work.

Acknowledgments

The authors are grateful for financial aids from the National Natural Science Foundation of China (Grant nos. 20372060, 20340420326 and 20490210) and the MOST of China ('973' Program, Grant no. 2006CB601103).

References

[1] T.M. Whitney, J.S. Jiang, P.C. Searson, C. Chien, Science 261 (1993) 1316.
[2] J.J. Versluijs, M.A. Bari, J.M.D. Coey, Phys. Rev. Lett. 87 (2001) 26601.
[3] K.V.P.M. Shafi, Y. Koltypin, A. Gedanken, R. Prozorov, J. Balogh, J. Lendvai, I.J. Felner, Phys. Chem. B 101 (1997) 6409.
[4] C. Jovalekic, M. Zdujic, A. Radakovic, M. Mitric, Mater. Lett. 24 (1995) 365.
[5] E. Manova, T. Tsoncheva, D. Paneva, I. Mitov, K. Tenchev, L. Petrov, Appl. Catal. A 119 (2004) 277.
[6] H. Yang, X. Zhang, A. Tang, G. Oiu, Chem. Lett. 33 (2004) 826.
[7] Y. Konishi, T. Kawamura, S. Asai, Ind. Eng. Chem. Res. 35 (1996) 320.
[8] T. Sugimoto, Y. Shimotsuma, H. Itoh, Powder Technol. 85 (1998) 96.
[9] J.C. Hoh, I.I. Yaacob, J. Mater. Res. 17 (2002) 3105.
[10] H. Tamura, E. Matijevic, J. Colloid Interface Sci. 90 (1982) 100.
[11] T. Pannaparayil, S. Komarneni, IEEE Trans. Magn. 25 (1989) 4233.
[12] X.F. Chu, D.L. Jiang, Y. Guo, C.M. Zheng, Sens. Actuators B 120 (2006) 177.
[13] Z.Y. Huo, C. Chen, Y.D. Li, Chem. Commun. (2006) 3522.
[14] G.B. Ji, S.L. Tang, S.K. Ren, F.M. Zhang, B.X. Gu, Y.W. Du, J. Cryst. Growth 270 (2004) 156.
[15] F. Tihay, A.C. Roger, G. Pourroy, A. Kiennemann, Energy Fuel 16 (2002) 1271.
[16] F. Tihay, A.C. Roger, A. Kiennemann, S. Lakamp, G. pourroy, Catal. Today 58 (2000) 263.
[17] T. Caillof, G. Pourroy, D. Stuerga, J. Solid State Chem. 177 (2004) 3843.
[18] A.E. Berkowitz, W.J. Schuele, J. Appl. Phys. 30 (1959) 1348.
[19] G. Wulff, Zeitschrift, F. Krystallogr. 34 (1901) 449.
[20] Z.L. Wang, J. Phys. Chem. B 104 (2000) 1153.
[21] M. Wu, Y. Xiong, Y. Jia, H. Niu, H. Qi, J. Ye, Q. Chen, Chem. Phys. Lett. 401 (2005) 374.
[22] H. Deng, X. Li, Q. Peng, X. Wang, J. Chen, Y. Li, Angew. Chem. Int. Ed. Engl. 44 (2005) 2782.
[23] Z.L. Wang, X. Feng, J. Phys. Chem. B 107 (2003) 13563.
[24] R.T. Olsson, G.S. Alvarez, M.S. He denqvist, U.W. Gedde, F. Lindberg, S.J. Savage, Chem. Mater. 17 (2005) 5109.
[25] S.H. Sun, H. Zeng, D.B. Robinson, S. Raoux, P.M. Rice, S.X. Wang, G.X. Li, J. Am. Chem. Soc. 126 (2004) 273.
[26] D. Caruntu, G. Caruntu, Y. Chen, C.J. O'Connor, G. Goloverda, V.L. Kolesnichenko, Chem. Mater. 16 (2004) 5527.
[27] B.J. Evans, S. Hafner, J. Phys. Chem. Solids 29 (1968) 1573.
[28] G. Pourroy, N. Viart, S. Läkamp, J. Magn. Magn. Mater. 203 (1999) 37.
[29] A.E. Berkowitz, W.J. Schuele, J. Appl. Phys. 30 (1959) 1345.
[30] A. E. Berkowitz, E. Kneller, Magnetism and metallurgy. Academic, New York, 1969. vol. 1, Chapter 8.